RSC Advances

PAPER

View Article Online
View Journal | View Issue

Cite this: *RSC Adv.*, 2019, **9**, 18222

Facile controlled synthesis of Ag_3PO_4 with various morphologies for enhanced photocatalytic oxygen evolution from water splitting†

Guiwei He, Wanliang Yang, * Wei Zheng, Li Gong, Xinghui Wang, Yan An and Mengkui Tian*

A facile and green hydrothermal method has been developed for the synthesis of Ag_3PO_4 with a variety of morphologies, including cubic, rhombic dodecahedral, spherical and roughly spherical, by using $Ag_4P_2O_7$ as a sacrificial precursor. The as-prepared catalysts were characterized by carrying out X-ray diffraction (XRD), scanning electron microscopy (SEM), UV-visible diffuse reflectance spectroscopy (UV-Vis DRS), Fourier transform infrared spectroscopy (FT-IR) and X-ray photoelectron spectroscopy (XPS). The morphology of Ag_3PO_4 was controlled by simply adjusting the hydrothermal reaction temperature and time, without adding any templates and organic additives. Kinetics studies and characterization results revealed that the transformation from $P_2O_7^{4-}$ to a PO_4^{3-} radical was a rate-determining step, and influenced the morphology of Ag_3PO_4. Different oxygen evolution rates were observed for samples subjected to different hydrothermal reaction times, and the highest initial rate of O_2 evolution achieved was 582.55 μmol h^{-1} g^{-1}. Furthermore, for the samples prepared using a hydrothermal reaction time of 96 h, as the hydrothermal reaction temperature was increased, the oxygen evolution rate of the resulting sample decreased first and then increased, and the highest initial rate of O_2 evolution was 856.06 μmol h^{-1} g^{-1}, about twice the 418.34 μmol h^{-1} g^{-1} value for the sample prepared using the coprecipitation method. A possible mechanism has been proposed to explain how the hydrothermal reaction temperature and time influenced the Ag_3PO_4 morphology. Our method provides a guiding hydrothermal strategy for the synthesis of insoluble electrolytes with various morphologies from relatively soluble electrolytes without the need to use templates and organic additives.

Received 21st February 2019
Accepted 10th May 2019

DOI: 10.1039/c9ra01306g

rsc.li/rsc-advances

Introduction

Semiconductor photocatalysis has garnered tremendous research interest in recent years, especially due to the developing shortage of fossil fuels and the accumulation of industrial sewage.[1–4] Multifarious traditional semiconductors such as TiO_2 have been confirmed to be outstanding photocatalysts for water-splitting and resulting H_2 production and for photodegradation.[5–7] Nevertheless, these wide-band photocatalysts only respond to ultraviolet light, which makes up less than 4% of the entire solar spectrum. In order to make the best use of solar energy, the exploitation of photocatalysts that can respond to visible light has become particularly important to produce electron–holes in a more efficient way.[8,9] Since silver phosphate (Ag_3PO_4) was first discovered by Ye in 2010, it has attracted great attention in the field of photocatalysis due to its proper band gap structure.[10] Many studies have been carried out to improve its photocatalytic activity and stability. Controlling the morphology of a photocatalyst is deemed to be one of the best methods to improve its photocatalytic activity.[11–13] For silver phosphate crystal catalysts, interfacial properties of the catalysts and reactants, such as specific surface area, exposed facets and photocurrent density, are determined by the sizes and morphologies of the crystals, which are the important parameters affecting photocatalytic activity.[11,14,15]

In recent years, many investigations have been devoted to further optimizing the photocatalytic activity and stability of Ag_3PO_4. Of these investigations, the morphology-controlled synthesis of Ag_3PO_4 has made notable progress, including towards the control of facets and the construction of multidimensional structures.[16,17] Photocatalysts with structures differing from those of their bulk counterparts have attracted considerable attention owing to their special chemical, electronic and optical properties.[18] The morphology of a photocatalyst is intimately related to the exposed facets, which directly influence the activity of photocatalyst. According to the crystal growth kinetic theory, the growth rate of seeds and the

School of Chemistry and Chemical Engineering, Guizhou University, Guiyang, Guizhou Province 550025, PR China. E-mail: yangwanlianghhhh@163.com; tianmk78@126.com; Tel: +86 15985159596; +86 18085027366

† Electronic supplementary information (ESI) available: More details of the SEM, FT-IR, XPS and UV-Vis of Ag_3PO_4 with various morphologies. See DOI: 10.1039/c9ra01306g

diffusion rate of precursors jointly determine the growth habit of crystals.[19,20] The growth habit can be adjusted by inorganic/organic additives, templates, reaction media and internal/external operating conditions, and such an adjustment ultimately results in changing the structural properties. Various Ag_3PO_4 nanostructures including spheres,[10,21] rhombic dodecahedrons,[22] concave trisoctahedrons,[23] cubes,[24] and tetrapods[17] with controlled particle sizes have been designed and synthesized to improve the photocatalytic properties further. For example, Ag_3PO_4 samples with different morphologies were synthesized by using three different precipitating agents (Na_3PO_4, Na_2HPO_4, and NaH_2PO_4) whose hydrolyses resulted in diverse solution pH values.[25,26] They have also been synthesized by using different organic additives, with these syntheses apparently proceeding according to the oriented aggregation mechanism: organic compounds containing Ag and a ligand complex were formed, followed by their having reacted with other compounds, then crystal nuclei having formed gradually and growing further, and finally with self-assembly and oriented aggregation having been realized. Different sizes and morphologies were produced using different templates such as polycarbonate membranes,[27] vinyl pyrrolidone (PVP),[28,29] and polyhedral Ag_3PO_4 microcrystals.[30] The prepared parameters including reaction components,[25,26] temperature, and time,[31] usually play a vital role in tailoring the morphologies and structures of Ag_3PO_4 crystals. In general, the area of reactive facets often decreases owing to the reduction of surface energy during the crystal growth process, which creates low-facet-energy crystals. Nevertheless, high-energy facets can be maintained under certain synthesis situations. Engineering the morphology as well as facets of the Ag_3PO_4 crystal have a great impact on its photocatalytic activity. There have been many reports about the synthesis of various forms of Ag_3PO_4. Unfortunately, organic solvents and/or capping agents are currently essential for adjusting the sizes and shapes of Ag_3PO_4 particles. As a result, there is an urgent need to develop a simple and environmentally friendly way to synthesize Ag_3PO_4 particles with various morphologies. Moreover, as far as we know, the use of related compounds such as $Ag_4P_2O_7$ in the synthesis of Ag_3PO_4 has hardly been studied so far.

In the current work, we explored a facile and green hydrothermal method without any templates and organic additives to carry out a shape-controlled synthesis of Ag_3PO_4 particles, with the procedure having them being transformed from rhombic dodecahedrons to spheres. The preparation was mainly divided into two stages. First, we made use of the synergetic reaction between silver cations and pyrophosphate anions to prepare $Ag_4P_2O_7$ nanoparticles. Secondly, the as-prepared silver pyrophosphate was used as a sacrificial precursor to prepare Ag_3PO_4 nanoparticles of various morphologies only by adjusting hydrothermal reaction time and temperature. The formation of these structures was systematically studied. The formation of rhombic dodecahedral Ag_3PO_4 carried out at a hydrothermal reaction temperature of 100 °C was indicated to involve a transformation from $Ag_4P_2O_7$ to Ag_3PO_4. The rhombic dodecahedral nanocrystals were transformed into spherical particles upon increasing the hydrothermal reaction temperature from 100 to 180 °C. A possible mechanism for the shape-controlled syntheses of Ag_3PO_4 was also proposed. In photocatalytic activity experiments that we carried out, the roughly spherical Ag_3PO_4 particles covered with small particles on their surfaces displayed better photocatalytic activity than did the other morphologies of Ag_3PO_4.

Experimental

Materials

All chemical agents used in the experiments were of analytical grade. Silver nitrate ($AgNO_3$) and disodium hydrogen phosphate (Na_2HPO_4, A.R.) was obtained from Sinopharm Chemical Reagent Co., Ltd. Sodium pyrophosphate ($Na_4P_2O_7$) was from Chengdu Jinshan Chemical Reagent Factory. Deionized water with a resistivity of 18.2 MΩ cm was used for aqueous solutions and photocatalytic activity tests.

Synthesis of Ag_3PO_4 using the coprecipitation method

A typical synthesis of Ag_3PO_4 using the coprecipitation method was carried out as follows. A mass of 2.7 g of $AgNO_3$ was scattered in 40 mL of deionized water, to which 40 mL of a solution of 0.2 M Na_2HPO_4 was then added. The resulting mixture was vigorously stirred for 5 h at 40 °C and then a yellow precipitate was obtained using filtration, washed with deionized water several times, and dried at 60 °C in air. This sample was marked as APO.

Synthesis of $Ag_4P_2O_7$

In the process used to synthesize $Ag_4P_2O_7$, first a mass of 2.7 g of $AgNO_3$ was dispersed in 40 mL deionized water, to which 40 mL of a solution of 0.1 M $Na_4P_2O_7$ was then added. The resulting mixture was vigorously stirred at 40 °C for 5 h, and then white precipitate was obtained using filtration, washed with deionized water several times, and dried at 60 °C in air.

Preparation of Ag_3PO_4 particles with different morphologies

The Ag_3PO_4 photocatalyst was prepared by using a simple hydrothermal method. In a typical process, a mass of 2.7 g of $AgNO_3$ was dissolved in 40 mL of deionized water, to which 40 mL of a solution of 0.1 M $Na_4P_2O_7$ was then added. The resulting mixture was vigorously stirred for 5 h at 40 °C, then transferred into a Teflon-lined autoclave and heated at 100 °C under autogenous pressure for 24 h, followed by being allowed to naturally cool to ambient temperature. The resulting product was separated using filtration, washed with deionized water three times and dried at 60 °C in air. Some Ag_3PO_4 samples were prepared by using different hydrothermal reaction times (24 h, 48 h, 72 h, 96 h) at 100 °C and were denoted as Ag_3PO_4 (t), and other Ag_3PO_4 samples were prepared by using different hydrothermal reaction temperatures (100, 120, 140, 160 and 180 °C) for 96 h, and were denoted as Ag_3PO_4 (T).

Characterizations

X-ray diffraction (XRD) patterns of the samples were recorded from a D8 Advance Focus diffractometer (Bruker) using Cu-Kα

radiation ($\lambda = 0.15405$ nm), in a 2θ angular range of 5–90°. The morphologies and sizes of the as-prepared products were characterized by using a field-emission scanning electron microscope (SEM) (S-3400N, HITACHI). The light absorption spectra of the samples were acquired when performing UV-visible diffuse reflection tests (UV-Vis, UV-3600 Plus, Shimadzu, Japan). The elemental composition and valence states of the samples were analyzed by carrying out X-ray photoelectron spectroscopy (XPS) (ThermoFisher K-Alpha, America). FTIR was applied to ascertain the chemical groups in Ag_3PO_4 photocatalysts. FTIR measurements were taken on a Nicolet IS50 infrared spectrometer after the sample was mixed with 300 mg of spectroscopic-grade KBr and pressed into thin slices.

Assessment of photocatalytic performance

The photocatalytic activities of the prepared productions were estimated by measuring the photocatalytic O_2 evolution under visible-light irradiation. The photocatalytic reaction was conducted in a Pyrex glass reactor at ambient temperature. A 300 W Xe arc lamp with a UV cut-off filter ($\lambda \geq 400$ nm) was used as the light source. A mass of 0.425 g of $AgNO_3$ was added into 110 mL of deionized water to form the mother solution used for the activity test, and then a mass of 0.1 g of as-prepared catalyst was dispersed into the above mixture as a sacrificial reagent. Then the above solution was subjected to ultrasonic dispersion for 3 min. The air in the reactor was replaced with Ar gas, which was irradiated by a 300 W Xe lamp with a cut-off filter ($\lambda \geq 400$ nm) under 15 °C circulating condensed water. A gas chromatograph was acquired (using an Agilent, 7820A, GC system) to detect the oxygen produced.

Results and discussion

We have developed a facile and green hydrothermal method to prepare Ag_3PO_4 with various morphologies by using silver pyrophosphate as a sacrificial precursor. The compositions and phase structures of all of the synthesized materials were determined from XRD measurements, and are shown in Fig. 1 and S1.† As shown in Fig. 1a, $Ag_4P_2O_7$ was obtained by using $AgNO_3$ and $Na_4P_2O_7$ as raw materials. Only one main peak ($2\theta = 32.4°$) appeared in the XRD pattern of the $Ag_4P_2O_7$ of JCPDS card no. 37-0187, because this sample was not mineralized at the 100 °C temperature used. In our experiments, when the hydrothermal reaction temperature was 100 °C and the hydrothermal reaction time was 24 h or 48 h, three strong peaks at 27.14°, 28.79°, and 32.4° were observed (Fig. 1a), and indicated the presence of $Ag_4P_2O_7$. The clear XRD pattern (see Fig. S1†) shows that the $P_2O_7^{4-}$ was present in the Ag_3PO_4 lattice. A peak was observed at 33.293°, which indicated that Ag_3PO_4 formed (JPCDS no. 06-0505), and hence that $Ag_4P_2O_7$ partly converted to Ag_3PO_4. The diffraction peaks corresponding to $Ag_4P_2O_7$ became weaker as the hydrothermal reaction time was increased, and disappeared after the reaction time was prolonged to 96 h. Here, no other peaks beside those corresponding to Ag_3PO_4 were observed (Fig. 1a, 96 h), indicating that a pure phase of the Ag_3PO_4 photocatalyst was obtained. It is notable that the peak intensity of Ag_3PO_4 became sharper and stronger with the increasing

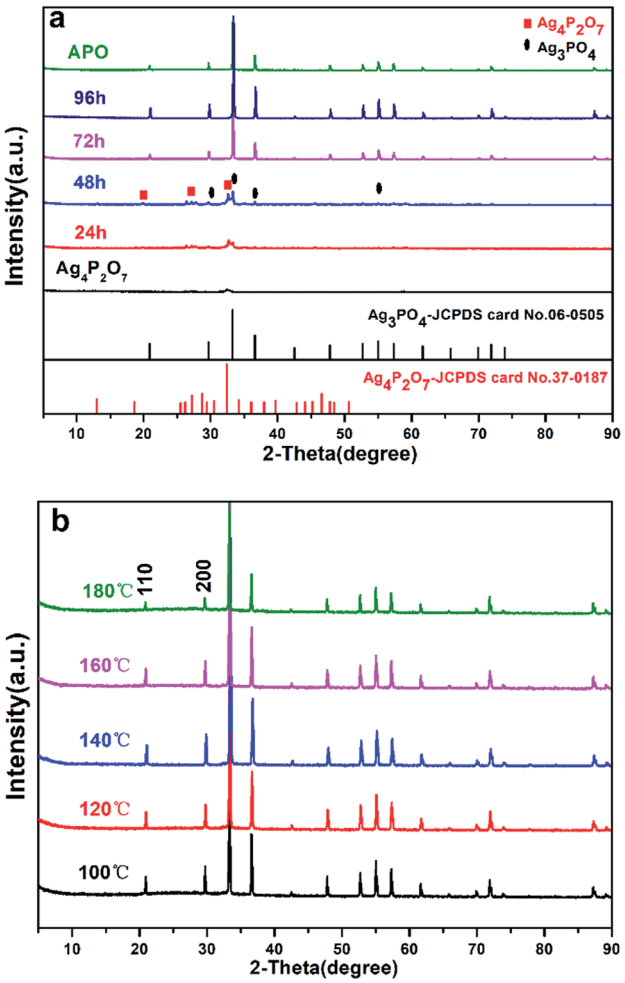

Fig. 1 XRD patterns of samples (a) at 100 °C and different hydrothermal reaction times: 24 h, 48 h, 72 h and 96 h, and (b) for 96 h and different hydrothermal reaction temperatures: 100 °C, 120 °C, 140 °C, 160 °C and 180 °C.

hydrothermal reaction time, which showed that $Ag_4P_2O_7$ was slowly converted to Ag_3PO_4. Furthermore, the peaks of the sample prepared for 96 h corresponded to the diffraction peak of Ag_3PO_4 (shown in Fig. 1b). The crystallinity of the as-prepared samples increased first as the hydrothermal reaction temperature was increased from 100 to 140 °C, and then decreased as the temperature was increased further to 180 °C (Fig. 1b), which may have been due to the destruction of crystals caused by the excessively high temperature.

The changes in the morphology and crystallinity of the synthesized Ag_3PO_4 were examined using SEM. The APO sample synthesized using the coprecipitation method presented as a spherical structure but whose particle size was not uniform (200–700 nm), as shown in Fig. 2-APO. As shown in Fig. 2 and S2,† while $Na_4P_2O_7$ was used as a precursor, the generated silver pyrophosphate formed a flaky polyhedron with an edge length of 100–300 nm and thickness of 30–40 nm (Fig. 2-$Ag_4P_2O_7$). For a hydrothermal reaction time of 24 h, Ag_3PO_4 cubes with approximately 600 nm-long edges were clearly observed, as shown in Fig. 3-24 h (Fig. S2-24 h†), and Ag_3PO_4 coexisted with $Ag_4P_2O_7$. With an

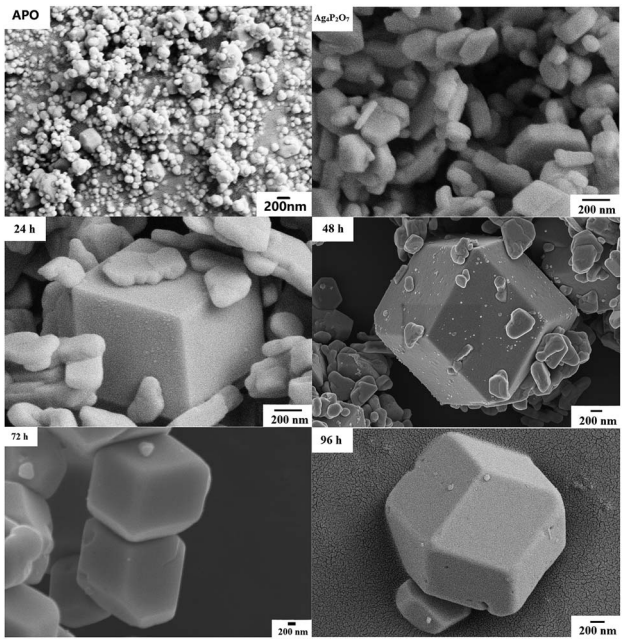

Fig. 2 SEM images of $Ag_4P_2O_7$, Ag_3PO_4 synthesized using the coprecipitation method (APO), and samples prepared at 100 °C but using different hydrothermal reaction times: 24 h, 48 h, 72 h and 96 h.

increase of the reaction time to 48 h, the $Ag_4P_2O_7$ still was present, but the Ag_3PO_4 cubes converted into rhombic dodecahedrons (Fig. 2-48 h and S2-48 h†). As shown in Fig. 2-72 h (Fig. S2-72 h†), no flaky silver pyrophosphate was observed when the hydrothermal reaction time was increased further to 72 h, and many Ag_3PO_4 rhombic dodecahedrons appeared. And for a reaction time of 96 h, the Ag_3PO_4 rhombic dodecahedrons with edge lengths of 300–600 nm were clearly observed (Fig. 2-96 h and S2-96 h†). The edges and corners of the pentagonal dodecahedrons were very clear, while the small flaky polyhedrons completely disappeared. The SEM data was consistent with the results of XRD (Fig. 1). The results taken together showed that, as the hydrothermal reaction time was increased, the $Ag_4P_2O_7$ dissolved, the $P_2O_7^{4-}$ converted gradually into PO_4^{3-} and then the silver phosphate was formed.

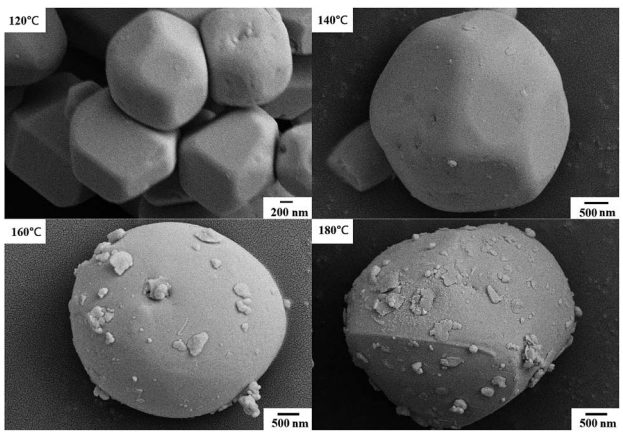

Fig. 3 SEM images of Ag_3PO_4 samples synthesized for 96 h at different hydrothermal temperatures: 100 °C, 120 °C, 140 °C, 160 °C and 180 °C.

The $Ag_4P_2O_7$ gradually converted to silver phosphate, but the diameters of the Ag_3PO_4 particles did not change significantly with changes in hydrothermal reaction time.[10,18,33,34] Furthermore, when the hydrothermal reaction time was set at 96 h, the edges and corners of the Ag_3PO_4 rhombic dodecahedrons gradually disappeared as the hydrothermal reaction temperature was increased from 100 °C to 180 °C (Fig. 3 and S3†). For example, when 120 °C was used, the edges and corners appeared somewhat blurry. And when a hydrothermal reaction temperature of 140 °C was used, hardly any complete surface of an Ag_3PO_4 dodecahedron was seen (Fig. 3-140 °C). Perhaps, at the higher hydrothermal reaction temperatures, the high specific surface energy of the fine particles predominated and caused the formation of roughly spherical particles.[35–37] In fact, spherical Ag_3PO_4 particles (3–5 μm) were clearly observed when a hydrothermal reaction temperature of 160 °C was used, and the surfaces of the silver phosphate particles became rough (Fig. 3-160 °C). This observation may be ascribed to the high hydrothermal reaction temperature having resulted in the small polyhedral silver phosphate particles falling onto the surface of the large particles of silver phosphate. When the hydrothermal reaction temperature was increased to 180 °C, the surfaces of the Ag_3PO_4 particles became even rougher (Fig. 3-180 °C). Such roughness may enhance their photocatalytic activity, because the small particles on the surface, being Ag_3PO_4, would increase the density of active sites on the surface and be beneficial to the contact of water molecules with the surface.[38–40] The FTIR spectra acquired from $Ag_4P_2O_7$, $Ag_4P_2O_7/Ag_3PO_4$ (48 h), and Ag_3PO_4 (96 h) are illustrated in Fig. S4.† Absorption bands at 908 and 1118 cm^{-1} were clearly observed, and ascribed to the symmetric stretching vibration of the P–O–P group of $Ag_4P_2O_7$, and another band was observed at 1108 cm^{-1}, and assigned to the presence of P–O. Also, three absorption bands appeared in $Ag_4P_2O_7/Ag_3PO_4$ (48 h), which resulted from the cleavage of some P–O–P bonds and the formation of P–O bonds. These results provided additional evidence that segmental $Ag_4P_2O_7$ converted to Ag_3PO_4, in accordance with the mechanism mentioned previously.

$$Na_4P_2O_7 + 4AgNO_3 \rightarrow Ag_4P_2O_7\downarrow + 4NaNO_3 \quad (1)$$

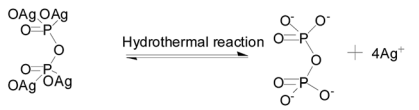

(2)

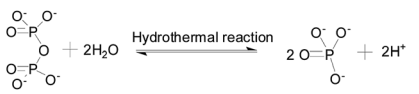

(3)

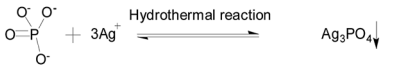

(4)

The above results clearly showed that Ag_3PO_4 materials with different morphologies can be successfully fabricated using the facile and green hydrothermal method. The morphology can be

controlled by simply tuning the hydrothermal reaction temperature and time without adding any templates and organic additives. We came up with a possible mechanism, shown in Fig. 4, to explain the formation of Ag_3PO_4 with various morphologies from the use of $Ag_4P_2O_7$ as a sacrificial precursor. Precipitation of $Ag_4P_2O_7$ finished instantly after the silver ions and pyrophosphate anions were mixed. The transformation of $P_2O_7^{4-}$ to a PO_4^{3-} radical has been indicated, using kinetics principles, to be a rate-determining step, which would result in different morphologies of Ag_3PO_4.

According to the proposed reaction mechanism for the formation of Ag_3PO_4, first $Ag_4P_2O_7$ formed when $AgNO_3$ was simply mixed with $Na_4P_2O_7$ at room temperature (eqn (1)). Then, the $Ag_4P_2O_7$ decomposed into pyrophosphate anions and silver ions to achieve equilibrium at a given temperature (eqn (2)). Eqn (3) shows a $P_2O_7^{4-}$ hydrolysis process in which PO_4^{3-} anions formed at a certain temperature. At last, silver phosphate formed when the hydrolyzed PO_4^{3-} anions combined with Ag^+ (eqn (4)).

To realize the transformation of the morphologies of Ag_3PO_4 from cubes to rhombic dodecahedrons, nearly equimolar quantities (four moles worth) of silver ions and pyrophosphate anions were mixed, and precipitates of silver pyrophosphate immediately formed. The obtained mixture was then transferred into a Teflon-lined autoclave and kept at 100 °C under autogenous pressure for different hydrothermal reaction times to synthesize Ag_3PO_4 particles with different morphologies. Because the conversion from $P_2O_7^{4-}$ to PO_4^{3-} in the solution proceeded extremely slowly, silver pyrophosphate converted into silver phosphate and the silver phosphate particles converted from flaky polyhedrons to rhombic dodecahedrons as the hydrothermal reaction time was increased. When the hydrothermal reaction temperature was increased gradually, the silver phosphate particles transformed from the rhombic dodecahedrons to spheres, and then to rough spheres.

The proposed mechanism of the growth of the Ag_3PO_4 particles with various morphologies is shown in Fig. 4. To begin with, precipitates of silver pyrophosphate immediately formed when silver ions and pyrophosphate anions were mixed at room temperature, and the silver pyrophosphate particles were observed to be flaky polyhedrons. When the hydrothermal reaction time was set at 24 h, some of the $Ag_4P_2O_7$ polyhedrons gradually transformed into Ag_3PO_4 cubes, which resulted in the simultaneous appearance of silver phosphate and silver pyrophosphate. As the hydrothermal reaction time was increased, much of the silver pyrophosphate gradually converted to cubic silver phosphate and then to rhombic dodecahedrons. With a further extension of the reaction time, silver pyrophosphate converted completely: that is, the transformation of the remaining silver pyrophosphate into rhombic dodecahedrons completed when the hydrothermal reaction time was increased to 96 h, and all the silver phosphate completely turned into rhombic dodecahedrons as well. All of the processes indicated that hydrothermal reaction time played a major role in the conversion of silver pyrophosphate to silver phosphate. The results also confirmed eqn (3) to be a rate-determining step in the transformation of $Ag_4P_2O_7$ to Ag_3PO_4. Furthermore, as the hydrothermal reaction temperature was raised from 100 to 180 °C, the rhombic dodecahedral silver phosphate gradually evolved into spheres, *i.e.*, the edges and corners disappeared. With a further increase of the hydrothermal reaction temperature, the surface of the sphere became rough, which indicated that the hydrothermal reaction

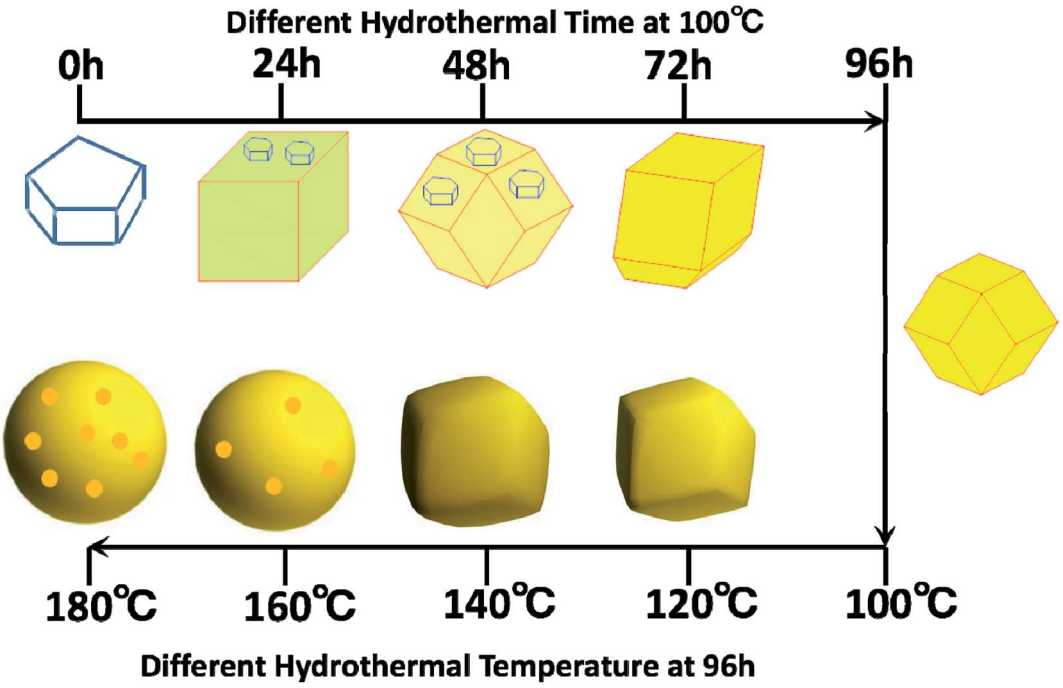

Fig. 4 Mechanism of formation of the samples with different morphologies at the various hydrothermal reaction temperatures and times.

temperature also functioned to change the morphology of the silver phosphate particle.[31,32]

To further confirm the proposed mechanism, we carried out XPS elemental analysis of $Ag_4P_2O_7$, $Ag_4P_2O_7/Ag_3PO_4$ (48 h at 100 °C), and Ag_3PO_4 (96 h at 100 °C), as shown in Fig. 5 and S5.† As $Ag_4P_2O_7$ transformed to Ag_3PO_4 with the increase of hydrothermal reaction time, the energy level of the 2p orbital of P shifted from 133.08 eV in $Ag_4P_2O_7$ to 132.58 eV in Ag_3PO_4 (Fig. 5a). Meanwhile, the binding energies of 1s orbitals of O varied from 530.88 eV to 530.48 eV (Fig. 5b). In contrast to these results for the $Ag_4P_2O_7$ and Ag_3PO_4 samples, the energy levels of the P 2p and O 1s peaks of the sample prepared for 48 h at 100 °C were observed at positions (Fig. 5c and d) between those observed for the $Ag_4P_2O_7$ and Ag_3PO_4 samples, suggesting that the sample prepared for 48 h at 100 °C contained both silver phosphate and silver pyrophosphate. The silver pyrophosphate molecule has, in addition to P═O and P–O bonds also found in Ag_3PO_4, a P–O–P bond not found in Ag_3PO_4. This difference apparently led to a difference in the molecular environments and measured binding energy levels of P and O between these two molecules. However, the binding energies of the Ag 3d orbitals were measured to be almost the same (Fig. S5†), although their peak intensities differed, attributed to the different amounts on the particle surface.[23,41,42] These conclusion are identical to the conclusions we arrived at as described above.

The UV-Vis analyses of the catalysts prepared with a hydrothermal reaction temperature set at 100 °C showed that the absorbance of the catalysts obviously red shifted as the hydrothermal reaction time was increased (Fig. 6a). Note that XRD results for a reaction time of 24 h indicated that the sample contained Ag_3PO_4, providing an explanation for the red shift of the sample in the UV-Vis spectrum. The absorbance intensities of Ag_3PO_4 prepared with reaction times of 72 h and 96 h were obviously greater than that of $Ag_4P_2O_7$ and the mixture phase in

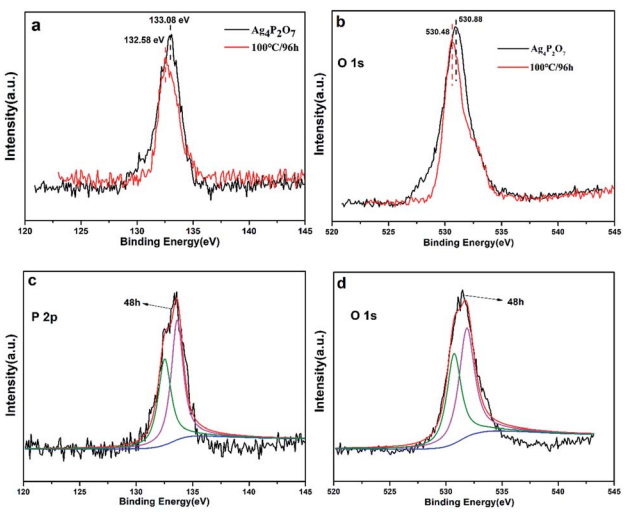

Fig. 5 XPS spectra of $Ag_4P_2O_7$, $Ag_4P_2O_7/Ag_3PO_4$ (48 h at 100 °C) and Ag_3PO_4 (96 h at 100 °C) samples: P 2p (a) and O 1s (b) regions for $Ag_4P_2O_7$ and Ag_3PO_4 (96 h at 100 °C), respectively; P 2p (c) and O 1s (d) regions for $Ag_4P_2O_7/Ag_3PO_4$ (48 h at 100 °C).

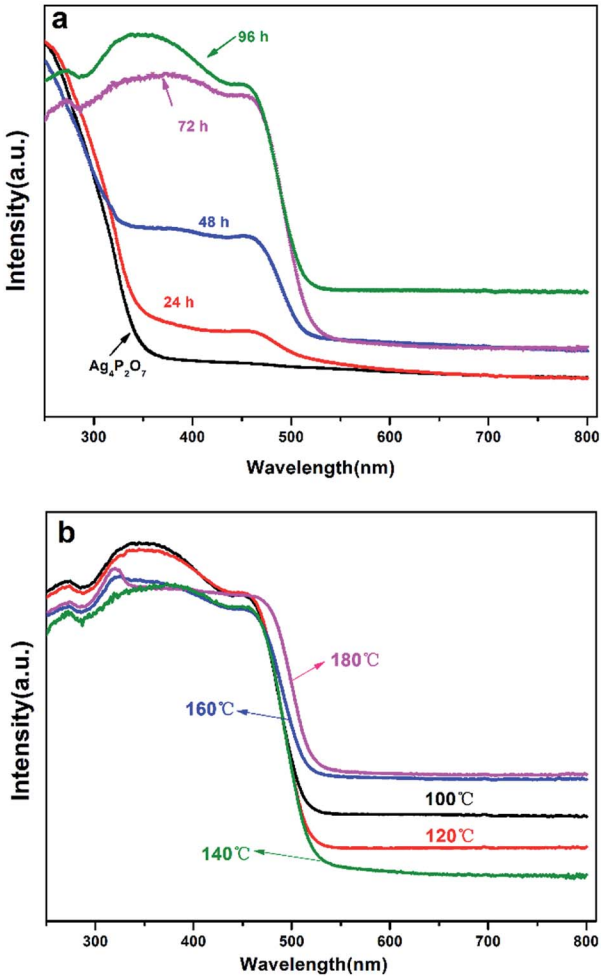

Fig. 6 Ultraviolet-visible diffusive reflectance spectra of the various catalyst samples prepared (a) at 100 °C for different hydrothermal reaction times, of 24 h, 48 h, 72 h and 96 h, and (b) for 96 h at different hydrothermal reaction temperatures, of 100 °C, 120 °C, 140 °C, 160 °C and 180 °C.

the 300–500 nm region. While in the 500–700 nm region, as the hydrothermal reaction time was increased, the catalyst showed an increased ability to absorb these wavelengths of light. When the hydrothermal reaction temperature was set at 100 °C, an obvious red shift in the UV-Vis spectrum was observed with the increase of hydrothermal reaction time during the transformation process from $Ag_4P_2O_7$ to Ag_3PO_4. Specifically, when the hydrothermal reaction times were 24 h and 48 h, there were two absorption band edges in the UV-Vis spectrum, which indicated that two different substances were present. Based on these results, combined with the above-described XRD (Fig. 1a) and SEM (Fig. 2) results, this phenomenon was concluded to have been caused by the coexistence of silver phosphate and silver pyrophosphate in the sample.[32] When the hydrothermal reaction times were 72 h and 96 h, the absorption band edge of $Ag_4P_2O_7$ was not obviously present, which indirectly indicated that all of the $Ag_4P_2O_7$ was converted to Ag_3PO_4 when the hydrothermal reaction time was 72 h. However, in the 500–700 nm wavelength absorption region, the intensity of the absorbance for the 96 h catalyst sample was significantly greater

than those of other catalysts. As mentioned above, this result was attributed to the obviously better absorbance displayed by the Ag_3PO_4 rhombic dodecahedron than by other catalysts with different morphologies.[10,43] In addition, Ag_3PO_4 is an indirect semiconductor.[44] And as can be seen from the UV-Vis spectra (Fig. 6), this indicated that no other impurity peaks formed. As shown in Fig. 6a and S6,† as the hydrothermal reaction time was increased, the absorption band edge was observed to increase from 357 nm to 533 nm, 546 nm, 536 nm, and finally to 540 nm; this result was ascribed to $Ag_4P_2O_7$ having converted to Ag_3PO_4 under these conditions. This transformation resulted in the red shift of the absorption band, thereby increasing the visible light response. According to the formula $E_g = 1240/\lambda_g$ (eV), where λ_g represents the threshold of the absorption wavelength, the corresponding band gaps were calculated to be 3.47 eV, 2.23 eV, 2.27 eV, 2.31 eV, 2.30 eV.[45,46]

As shown in Fig. 6b, controlled the hydrothermal time at 96 hours, when the temperature is lower than 140 °C, the absorption band edge of the sample is almost unchanged, all of which are around 533 nm, which fully illustrates only Ag_3PO_4, no other impurities exists in the catalyst.[43] However, when the temperature is higher than 160 °C, the surface of Ag_3PO_4 becomes rough, which results in partial red shift of its absorption edge. However, it can be seen that the intensity of the absorbance first decreased and then increased gradually with the increase of the hydrothermal reaction temperature in the region of 500–700 nm. Especially when the hydrothermal reaction temperature was below 140 °C, the intensity of the absorbance in this region tended to decrease with the increasing reaction time, and this result may have been due to the transformation from rhombic dodecahedral Ag_3PO_4 particles into spherical Ag_3PO_4 particles. When the hydrothermal reaction temperature was higher than 140 °C, the intensity of the absorbance in this region tended to increase with the increasing reaction time, and as mentioned above, this result may have been due to the surfaces of the spherical Ag_3PO_4 particles having become coarse.[43]

To assess the photocatalytic activities of the different Ag_3PO_4 samples, $AgNO_3$ was used as a sacrificial reagent. For comparison, all of the performance tests were carried out with 0.425 g $AgNO_3$ dissolved in 110 mL deionized water as a sacrificial reagent and added 0.1 g catalyst, and with other conditions remaining the same. Fig. 7a shows a diagram of the oxygen production of the photocatalysts prepared at 100 °C but with different hydrothermal reaction times. Here, the oxygen production levels of the samples clearly increased with increasing hydrothermal reaction time. The rate of oxygen evolution catalyzed by Ag_3PO_4 was 582.55 μmol h^{-1} g^{-1} when

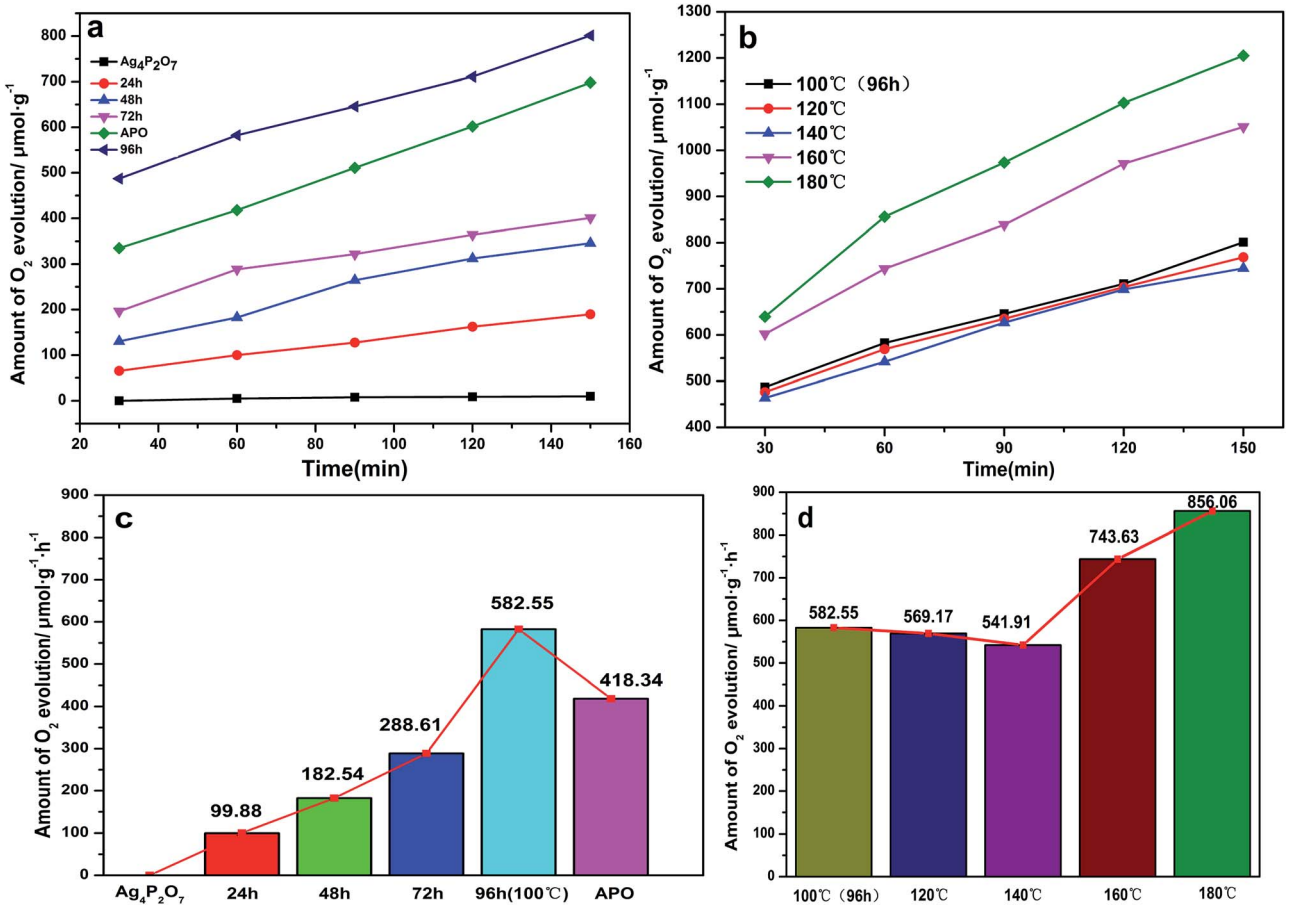

Fig. 7 Photocatalytic activities of Ag_3PO_4 samples under visible light for the evolution of O_2 from an aqueous $AgNO_3$ solution. (a) Different hydrothermal reaction times for the 100 °C preparation. (b) Different hydrothermal reaction temperatures for the 96 h preparation. (c) Histogram of oxygen production of the 100 °C as-prepared samples. (d) Histogram of oxygen production of 96 h as-prepared samples.

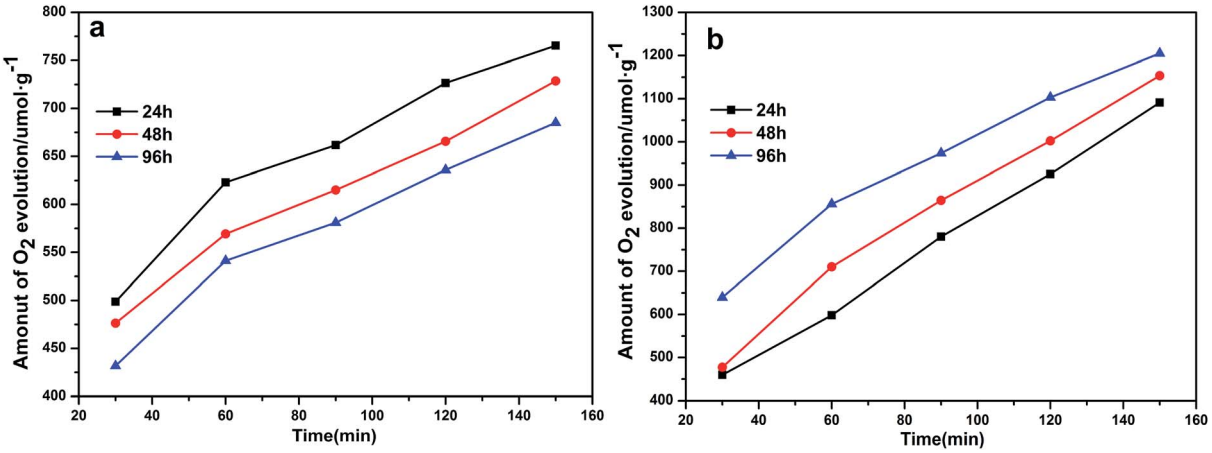

Fig. 8 Photocatalytic activities of Ag_3PO_4 samples under visible light for O_2 evolution from an $AgNO_3$ aqueous solution. (a) Various hydrothermal reaction times for a hydrothermal reaction temperature of 120 °C. (b) Various hydrothermal reaction times for a hydrothermal reaction temperature of 180 °C.

the hydrothermal reaction time was 96 h. This result was due to the generation of rhombic dodecahedral Ag_3PO_4 with excellent activity when the hydrothermal reaction time was increased to this level.[22,31,47] Note that the oxygen production rate of APO was measured to be 418.34 μmol h^{-1} g^{-1}, and the results discussed above illustrated that the photocatalytic activity of rhombic dodecahedral Ag_3PO_4 exceeded that of a sphere. As shown in Fig. 7b, when the hydrothermal reaction time was set at 96 h and the hydrothermal reaction temperature was increased, the oxygen production rate decreased first and then increased. The rates of oxygen production for Ag_3PO_4 (140 °C) and Ag_3PO_4 (180 °C) were 541.91 μmol h^{-1} g^{-1} and 856.06 μmol h^{-1} g^{-1} when the hydrothermal reaction temperatures were set at 140 °C and 180 °C, indicating that the oxygen production capacity of the Ag_3PO_4 sample made using a hydrothermal reaction temperature of 180 °C was obviously stronger than those of the samples made using other reaction temperatures. This result was attributed to the active facet with large Gibbs free energy on the surface gradually disappearing with the increase of hydrothermal reaction temperature. The exposed facet of the semiconductor will greatly affect the photocatalytic activity of the semiconductor; and especially for the {110} and {100} facets of silver phosphate, a higher facet activation energy results in better catalytic activity. The disappearance of the active facets of the rhombic dodecahedron caused the activity of the sample to decrease. As can be seen in Fig. 5, the spherical surface of the Ag_3PO_4 (180 °C) particles appeared rough, due to the deposition of small silver phosphate particles on the surfaces of the spherical silver phosphate particles.[45,48] The decrease in the average size of the Ag_3PO_4 particles greatly increased the relative surface area of the particles and hence the quantity of active sites on the surfaces, features beneficial for the catalytic activity of spherical silver phosphate particles and that helped make the resulting oxygen production become more vigorous.[41,42,49,50] In order to confirm the superiority of rhombic dodecahedral Ag_3PO_4 particle, it can be inferred that the decline of photocatalytic activity resulted from the disappearance of {110} when the hydrothermal reaction temperature was set at 120 °C (Fig. 8a). In addition, the photocatalytic activity increased along with the increase in surface roughness when the hydrothermal reaction temperature was set at 180 °C (Fig. 8b).

Pure Ag_3PO_4 exhibited a strong oxygen evolution ability according to the previous study[10] (see Fig. 9). The valence band of Ag_3PO_4 was determined to be mainly composed of O 2p and Ag 4d, and the conduction band was determined to be mainly composed of Ag 5s, leading to the dispersion of many Ag s orbitals on the adjacent orbitals, in turn leading to the absence of Ag orbitals at the bottom of the conduction band, a feature also effective for dispersing Ag in s orbitals. The reduction of the total mass of effective electrons has been indicated to result in an increase in the separation effect of the photoelectrons. Moreover, the bottom of the conduction band of Ag_3PO_4 was shown to display an isotropic distribution, a feature also beneficial for the transfer of electrons and for

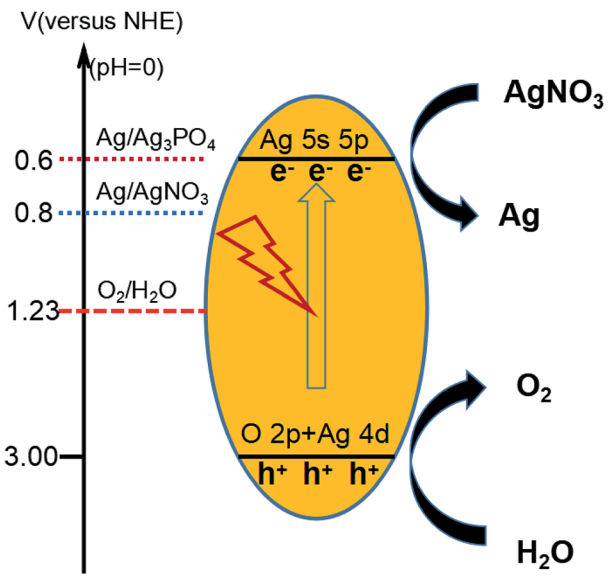

Fig. 9 Schematic drawing of redox potentials of Ag_3PO_4 and the mechanism of O_2 evolution.

increasing the photocatalytic activity.[11–13,44,51–53] The strategy in which pyrophosphate was used as a precursor to prepare silver phosphate not only enriched the synthetic routes to Ag_3PO_4, but also provided a novel means to enhance the stability of Ag_3PO_4.

Conclusions

Ag_3PO_4 samples with different morphologies were prepared through the *in situ* conversion of Ag^+ to $Ag_4P_2O_7$ nanocrystals assisted by pyrophosphate anions, followed by the oriented attachment of the nanocrystals to form Ag_3PO_4 crystals with specific shapes determined by the hydrothermal reaction temperature and time used. The simple synthetic process used involved neither templates nor organic additives, and $Ag_4P_2O_7$ nanocrystals functioned as not only sacrificial templates but also the source of Ag and phosphate anions for the generation of Ag_3PO_4 crystals. The hydrothermal reaction temperature and time were the predominant factors that were used to control the morphologies of the Ag_3PO_4 crystals, which in this way could be varied from nanoparticles to cubes, rhombic dodecahedrons, spheres and rough spheres. Photocatalytic oxygen production tests demonstrated that rough-spherical Ag_3PO_4 particles covered with small particles exhibited the best initial oxygen evolution rate of about 856 μmol h^{-1} g^{-1}, and hence the most outstanding activity of all the photocatalyst samples tested. The second best Ag_3PO_4 catalytic activity was observed for spheres, third best for dodecahedrons, and lastly $Ag_4P_2O_7$ nanocrystals. These observations can be explained by the visible light absorption capability and structural factors of these photocatalysts. This work has provided a new understanding of how to design highly efficient oxygen production photocatalysts displaying various morphologies. We believe that such a facile and green approach could also be used to prepare other insoluble electrolytes materials.

Conflicts of interest

There are no conflicts to declare.

Acknowledgements

This work was supported by the Science and Technology Planning Project of Guizhou Province [2017]5788-56, the Talent Introduction Program of Guizhou University (GDRJH2014-23 and GDRJH2014-21), Natural Science Foundation of China (No. 21663009), the Excellent Youth Fund of Guizhou Province [2017]5605 and Platform & Talent Program from Guizhou Province [2017]5788.

Notes and references

1 C. Jiang, S. J. A. Moniz, A. Wang, T. Zhang and J. Tang, *Chem. Soc. Rev.*, 2017, **46**, 4645–4660.
2 S. J. A. Moniz, S. A. Shevlin, D. J. Martin, Z.-X. Guo and J. Tang, *Energy Environ. Sci.*, 2015, **8**, 731–759.
3 S. Subudhi, D. Rath and K. M. Parida, *Catal. Sci. Technol.*, 2018, **8**, 679–696.
4 B. Zhu, R. Zou and Q. Xu, *Adv. Energy Mater.*, 2018, **8**, 1801193.
5 X. Chen, S. Shen, L. Guo and S. S. Mao, *Chem. Rev.*, 2010, **110**, 6503–6570.
6 L. Cheng, Q. Xiang, Y. Liao and H. Zhang, *Energy Environ. Sci.*, 2018, **11**, 1362–1391.
7 X. Li, J. Yu and M. Jaroniec, *Chem. Soc. Rev.*, 2016, **45**, 2603–2636.
8 X. Chen, L. Liu and F. Huang, *Chem. Soc. Rev.*, 2015, **44**, 1861–1885.
9 Y. Liu, L. Tian, X. Tan, X. Li and X. Chen, *Sci. Bull.*, 2017, **62**, 431–441.
10 Z. Yi, J. Ye, N. Kikugawa, T. Kako, S. Ouyang, H. Stuart-Williams, H. Yang, J. Cao, W. Luo, Z. Li, Y. Liu and R. L. Withers, *Nat. Mater.*, 2010, **9**, 559–564.
11 X. Chen, Y. Dai and X. Wang, *J. Alloys Compd.*, 2015, **649**, 910–932.
12 G. Huang, Z.-L. Ma, W.-Q. Huang, Y. Tian, C. Jiao, Z.-M. Yang, Z. Wan and A. Pan, *J. Nanomater.*, 2013, **9**, 1–8.
13 D. J. Martin, G. Liu, S. J. A. Moniz, Y. Bi, A. M. Beale, J. Ye and J. Tang, *Chem. Soc. Rev.*, 2015, **44**, 7808–7828.
14 D. Wang, T. Hisatomi, T. Takata, C. Pan, M. Katayama, J. Kubota and K. Domen, *Angew. Chem., Int. Ed.*, 2013, **52**, 11252–11256.
15 Y. Xia, Y. Xiong, B. Lim and S. E. Skrabalak, *Angew. Chem., Int. Ed.*, 2009, **48**, 60–103.
16 M.-S. Hsieh, H.-J. Su, P.-L. Hsieh, Y.-W. Chiang and M. H. Huang, *ACS Appl. Mater. Interfaces*, 2017, **9**, 39086–39093.
17 J. Wang, F. Teng, M. Chen, J. Xu, Y. Song and X. Zhou, *CrystEngComm*, 2013, **15**, 39–42.
18 K. Zhou and Y. Li, *Angew. Chem., Int. Ed.*, 2012, **51**, 602–613.
19 R. Agarwal, *Small*, 2008, **4**, 1872–1893.
20 M. J. Bierman, Y. K. A. Lau, A. V. Kvit, A. L. Schmitt and S. Jin, *Science*, 2008, **320**, 1060–1063.
21 L. Wang, L. Wang, D. Chu, Z. Wang, Y. Zhang and J. Sun, *Catal. Commun.*, 2017, **88**, 53–55.
22 Y. Bi, S. Ouyang, N. Umezawa, J. Cao and J. Ye, *J. Am. Chem. Soc.*, 2011, **133**, 6490–6492.
23 Z. Jiao, Y. Zhang, H. Yu, G. Lu, J. Ye and Y. Bi, *Chem. Commun.*, 2013, **49**, 636–638.
24 Y. Bi, H. Hu, S. Ouyang, G. Lu, J. Cao and J. Ye, *Chem. Commun.*, 2012, **48**, 3748–3750.
25 P. Amornpitoksuk, K. Intarasuwan, S. Suwanboon and J. Baltrusaitis, *Ind. Eng. Chem. Res.*, 2013, **52**, 17369–17375.
26 X. Song, R. Li, M. Xiang, S. Hong, K. Yao and Y. Huang, *Ceram. Int.*, 2017, **43**, 4692–4701.
27 C.-T. Dinh, T.-D. Nguyen, F. Kleitz and T.-O. Do, *Chem. Commun.*, 2011, **47**, 7797–7799.
28 Y. Bi, H. Hu, Z. Jiao, H. Yu, G. Lu and J. Ye, *Phys. Chem. Chem. Phys.*, 2012, **14**, 14486–14488.
29 Q. Cao, J. Yu, K. Yuan, M. Zhong and J.-J. Delaunay, *ACS Appl. Mater. Interfaces*, 2017, **9**, 19507–19512.
30 P. Dong, Y. Wang, H. Li, H. Li, X. Ma and L. Han, *J. Mater. Chem. A*, 2013, **1**, 4651–4656.

31 X. Guan, J. Shi and L. Guo, *Int. J. Hydrogen Energy*, 2013, **38**, 11870–11877.
32 Z. Wang, Y. Inoue, T. Hisatomi, R. Ishikawa, Q. Wang, T. Takata, S. Chen, N. Shibata, Y. Ikuhara and K. Domen, *Nat. Catal.*, 2018, **1**, 756–763.
33 X. Yang, H. Cui, Y. Li, J. Qin, R. Zhang and H. Tang, *ACS Catal.*, 2013, **3**, 363–369.
34 G. A. Somorjai and D. W. Blakely, *Nature*, 1975, **258**, 580–583.
35 H. Hu, Z. Jiao, H. Yu, G. Lu, J. Ye and Y. Bi, *J. Mater. Chem. A*, 2013, **1**, 2387–2390.
36 D. J. Martin, N. Umezawa, X. Chen, J. Ye and J. Tang, *Energy Environ. Sci.*, 2013, **6**, 3380–3386.
37 G.-Y. Zhang, X.-M. Wei, X. Bai, C.-M. Liu, B.-Y. Wang and J.-W. Liu, *Inorg. Chem. Front.*, 2018, **5**, 951–961.
38 Y. Bi, H. Hu, S. Ouyang, Z. Jiao, G. Lu and J. Ye, *Chem. - Eur. J.*, 2012, **18**, 14272–14275.
39 Y. Bi, H. Hu, S. Ouyang, Z. Jiao, G. Lu and J. Ye, *J. Mater. Chem.*, 2012, **22**, 14847–14850.
40 C. Li, P. Zhang, R. Lv, J. Lu, T. Wang, S. Wang, H. Wang and J. Gong, *Small*, 2013, **9**, 3951–3956.
41 Q. Guo, H. Li, Q. Zhang and Y. Zhang, *Appl. Catal., B*, 2018, **229**, 192–203.
42 J. Tian, T. Yan, Z. Qiao, L. Wang, W. Li, J. You and B. Huang, *Appl. Catal., B*, 2017, **209**, 566–578.
43 Q. Liang, W. Ma, Y. Shi, Z. Li and X. Yang, *CrystEngComm*, 2012, **14**, 2966–2973.
44 N. Umezawa, O. Shuxin and J. Ye, *Phys. Rev. B: Condens. Matter Mater. Phys.*, 2011, **83**, 035202–035210.
45 W. Zhang, R. Zhu, L. Ke, X. Liu, B. Liu and S. Ramakrishna, *Small*, 2010, **6**, 2176–2182.
46 F. Pang, X. T. Liu, M. Y. He and J. P. Ge, *Nano Res.*, 2015, **8**, 106–116.
47 B. Zheng, X. Wang, C. Liu, K. Tan, Z. Xie and L. Zheng, *J. Mater. Chem. A*, 2013, **1**, 12635–12640.
48 Z.-M. Yang, G.-F. Huang, W.-Q. Huang, J.-M. Wei, X.-G. Yan, Y.-Y. Liu, C. Jiao, Z. Wan and A. Pan, *J. Mater. Chem. A*, 2014, **2**, 1750–1756.
49 X. Guan and L. Guo, *ACS Catal.*, 2014, **4**, 3020–3026.
50 S. Huang, Y. Xu, Q. Liu, T. Zhou, Y. Zhao, L. Jing, H. Xu and H. Li, *Appl. Catal., B*, 2017, **218**, 174–185.
51 X. L. F. J. J. Liu, S. F. Chen and Y. F. Zhu, *Appl. Phys. Lett.*, 2011, **99**, 191903.
52 X. Ma, B. Lu, D. Li, R. Shi, C. Pan and Y. Zhu, *J. Phys. Chem. C*, 2011, **115**, 4680–4687.
53 P. Reunchan and N. Umezawa, *Phys. Rev. B: Condens. Matter Mater. Phys.*, 2013, **87**, 245205–245210.